CHEMISTRY OF MATERIALS

Article

pubs.acs.org/cm

$Rb_jM_k[Fe(CN)_6]_l$ (M = Co, Ni) Prussian Blue Analogue Hollow Nanocubes: a New Example of a Multilevel Pore System

Olivia N. Risset,[†] Elisabeth S. Knowles,[‡] Shengqian Ma,[§] Mark W. Meisel,[‡] and Daniel R. Talham*[,†]

[†]Department of Chemistry, University of Florida, Gainesville, Florida 32611-7200, United States

[‡]Department of Physics and the National High Magnetic Field Laboratory, University of Florida, Gainesville, Florida 32611-8440, United States

[§]Department of Chemistry, University of South Florida, Tampa, Florida 33620-5250, United States

Supporting Information

ABSTRACT: A facile surfactant-free route to synthesize uniform $Rb_{0.4}M_4[Fe(CN)_6]_{2.8}\cdot 7.2H_2O$ (M = Co, Ni) hollow nanoparticles is described. $Rb_{1.6}Mn_4[Fe(CN)_6]_{3.2}\cdot 4.8H_2O$ serves as a sacrificial/removable core in the synthesis of core@shell heterostructures. After dissolution of the cores under very mild conditions, the crystalline hollow nanocubes feature well-defined micro-, meso-, and macropores. The surfactant-free approach preserves the reactivity of the Prussian blue analogue surface as evidenced by the subsequent synthesis of hollow shell@shell heterostructures.

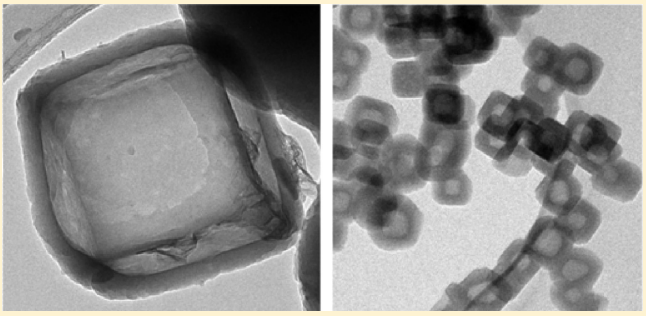

KEYWORDS: *Prussian blue analogue nanoparticles, hollow nanocubes, coordination polymer heterostructures, hierarchical pore system*

INTRODUCTION

Since the 1990s, the prolific development of nanoporous materials has extended their application range beyond traditional uses in ion exchange, adsorptive separation, and catalysis.[1,2] Increased control over the distribution of sizes, shapes, and volumes of the void spaces has opened up new opportunities in fields as diverse as medical diagnosis and imaging, drug delivery, lithium-ion batteries, optics, and photonics. Among porous materials, hierarchical systems with ordered micro-, meso-, and even macropores have attracted a growing interest because of the potential to optimize properties arising from a complex multilevel architecture.[3,4]

The last 10 years have seen tremendous progress in the synthesis of hollow structured materials.[5] The macroscale internal cavities of hollow particles when coupled with nanoporous shells exemplify the concept of hierarchical pore systems and lead to materials with high specific surface area, low density and surface permeability.[6] Recently, Lou and coworkers reported SnO_2 hollow structures with enhanced lithium storage capacity and improved cyclability.[7,8] Hollow mesoporous nanospheres used as carriers for controlled drug release have also showed promising results demonstrating the wealth of properties originating from the unusual hollow morphology.[9]

The most popular strategy to achieve hollow structures involves the coating of a shell on removable or sacrificial templates. This "template approach" has proven very effective in the synthesis of a wide variety of hollow particles.[5] Diverse and versatile templates are available ranging from hard silica spheres[10,11] or metallic nanoparticles[12,13] to soft emulsion droplets[6,14] or gas bubbles.[15] Template methods possess major advantages in control over the size and shape of the products. However, they also have some inherent drawbacks attributed to tedious synthetic procedures. For example, the removal of hard templates often requires calcination or chemical etching with hazardous chemicals such as hydrofluoric acid. The harsh treatment can lead to partial collapse of the hollow structures, significantly affecting the quality and properties of the hollow particles.

Promising materials for the design of hollow shells are porous coordination polymers (PCPs).[6,16−19] Owing to their large and uniform porosity,[20,21] PCPs are attractive materials in applications that require selective permeability. Even though PCP films have demonstrated outstanding properties in optics, gas separation, and sensors,[22,23] PCPs with complex morphologies such as hollow structures and more exotic multilevel interior designs are scarce.[3]

Prussian blue analogues (PBAs) are a widely studied family of PCPs.[24] PBAs adopt cubic structures of formula $A_{4x}M_4[M'(CN)_6]_{4z}\square_{4(1-z)}\cdot yH_2O$ where M^{n+} and M'^{m+} are metal ions linked by cyanide ligands in an octahedral fashion and $x = [(6 - m)z] - n$ (Figure 1).[25] The presence of alkali metal cations A^+ and/or intrinsic vacancies $\square$ ensures the electroneutrality of the compound. For $z < 1$, water molecules complete the coordination spheres of M centers adjacent to the vacant M′ sites. Zeolitic water molecules and alkali ions occupy

Received: September 17, 2012
Revised: December 3, 2012
Published: December 8, 2012

 © 2012 American Chemical Society dx.doi.org/10.1021/cm302995w | *Chem. Mater.* 2013, 25, 42−47

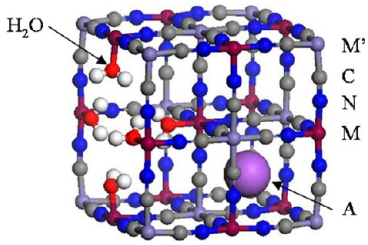

Figure 1. Scheme of the PBA cubic structure. Zeolitic water molecules are omitted for clarity.

the interstitial sites. The field of PBA-based nanoparticles has significantly expanded over the last 10 years, from the development of microemulsion techniques[26,27] to the preparation of self-stabilized colloidal suspensions.[28] Fine control over the size and composition of the particles has been achieved, allowing for the design of even more complex architectures such as core@shell heterostructures.[29−31] Recently, Wang and coworkers[17,32] and Roy et al.[19] developed elegant methods for the synthesis of PBA hollow nanostructures. The nanoshells are prepared by using an organometallic directing agent to control the growth and stabilize the surface of the particles. Furthermore, Hu et al. reported the synthesis of PBA hollow shells by controlled chemical etching in the presence of polyvinylpyrrolidone as a coating agent.[33,34]

Herein, we describe the synthesis of uniform hollow PBA nanocubes of formula $Rb_{0.4}M_4[Fe(CN)_6]_{2.8}\cdot 7.2H_2O$ (M = Co or Ni) using a sacrificial/removable template approach. Core@shell heterostructures $Rb_{1.6}Mn_4[Fe(CN)_6]_{3.2}\cdot 4.8H_2O$@ $Rb_{0.4}M_4[Fe(CN)_6]_{2.8}\cdot 7.2H_2O$ are first synthesized and the cores are dissolved under mild conditions that prevent the hollow particles from collapsing. This surfactant-free route yields hollow shells with a surface that remains chemically active, as evidenced by the subsequent synthesis of hollow shell@shell heterostructures. The crystalline nanoboxes are a new example of hierarchical PCPs featuring micro-, meso-, and macropores.

EXPERIMENTAL SECTION

Material Preparation. All chemical reagents were purchased from Sigma-Aldrich and used without further purification. The nanoparticles were filtered on rapid-flow bottle top filters with 0.45 μm pore size PES membrane (Nalgene).

Core Particles. In a typical experiment, 50 mL of an aqueous solution of $MnCl_2.4H_2O$ (99 mg; 0.50 mmol) were added dropwise (2.5 mL/min) to an equal volume of an aqueous solution containing $K_3[Fe(CN)_6]$ (181 mg; 0.55 mmol) and RbCl (181 mg; 1.50 mmol). After maturation for 4 h under vigorous stirring, the particles were filtered under vacuum using a 0.45 μm filter and redispersed in 250 mL of a water/methanol mixture (4:1) to give the suspension of core particles. Except for a 1 mL aliquot used for characterization, the particles were not isolated and the suspension was used immediately in the next step.

$Rb_{1.6}Mn_4[Fe(CN)_6]_{3.2}\cdot 4.8H_2O$ (RbMnFe). Deep brown powder. IR (KBr):[35] 2151 (νCN, Mn^{II}−NC−Fe^{III}), 2080 (νCN, Mn^{III}−NC−Fe^{II}) cm^{-1}. EDS: 0.4:1:0.8 (Rb:Mn:Fe).

Core@Shell Particles. Core@shell particles were synthesized using a modification of the method reported by Dumont et al.[30] $MCl_2.6H_2O$ (M = Co or Ni; 100 mg; 0.42 mmol) and RbCl (100 mg; 0.83 mmol) dissolved in 100 mL of a water/methanol mixture (4:1) and an equal volume of the same solvent mixture containing $K_3[Fe(CN)_6]$ (66 mg; 0.20 mmol to form RbCoFe/50 mg; 0.15 mmol to form RbNiFe) were simultaneously added (8 mL/h using a peristaltic pump) to the core particle suspension under vigorous stirring for 18 h. The product was filtered under vacuum using a 0.45 μm filter. Except for a 1 mL aliquot used for characterization, the particles were not isolated and treated immediately as described in the next step.

$Rb_{1.6}Mn_4[Fe(CN)_6]_{3.2}\cdot 4.8H_2O$@$Rb_{0.4}Co_4[Fe(CN)_6]_{2.8}\cdot 7.2H_2O$ (RbMnFe@RbCoFe). Deep purple powder. IR (KBr):[36] 2152 (νCN, Mn^{II}−NC−Fe^{III}, Co^{II}−NC−Fe^{III} high spin (HS)), 2109 (νCN, Co^{II}−NC−Fe^{III} low spin (LS)), Co^{II}−NC−Fe^{II}), 2080 (νCN, Mn^{III}−NC−Fe^{II}) cm^{-1}. EDS: 0.4:1:0.8 (Rb:Mn:Fe), 0.1:1:0.7 (Rb:Co:Fe), 1.6:1 (Mn:Co).

$Rb_{1.6}Mn_4[Fe(CN)_6]_{3.2}\cdot 4.8H_2O$@$Rb_{0.4}Ni_4[Fe(CN)_6]_{2.8}\cdot 7.2H_2O$ (RbMnFe@RbNiFe). Yellow powder. IR (KBr):[37] 2152 (νCN, Mn^{II}−NC−Fe^{III}, Ni^{II}−NC−Fe^{III}), 2099 (νCN, Ni^{II}−NC−Fe^{II}), 2077 (νCN, Mn^{III}−NC−Fe^{II}) cm^{-1}. EDS: 0.4:1:0.8 (Rb:Mn:Fe), 0.1:1:0.7 (Rb:Ni:Fe), 0.9:1 (Mn:Ni).

Hollow particles. The core@shell particles were allowed to stir in 1 L of water at 45 °C for 45 min. The product was then filtered using a 0.45 μm filter and the procedure was repeated twice. The particles were filtered one last time, redispersed in a minimum amount of water and air-dried. For each product, the yield was calculated from the maximum theoretical amount determined by the quantity of divalent metal salt introduced.

$Rb_{0.4}Co_4[Fe(CN)_6]_{2.8}\cdot 7.2H_2O$ (RbCoFe). Purple powder (83 mg; 80% yield). IR (KBr): 2159 (νCN, Co^{II}−NC-Fe^{III} high spin (HS)), 2109 (νCN, Co^{II}−NC−Fe^{III} low spin (LS)), 2095 (νCN, Co^{II}−NC−Fe^{II}) cm^{-1}. EDS: 0.1:1:0.7 (Rb:Co:Fe).

$Rb_{0.4}Ni_4[Fe(CN)_6]_{2.8}\cdot 7.2H_2O$ (RbNiFe). Yellow powder (79 mg; 78% yield). IR (KBr): 2165 (νCN, Ni^{II}−NC-Fe^{III}), 2124 (νCN, Ni^{II}−NC-Fe^{III} terminal) 2099 (νCN, Ni^{II}−NC-Fe^{II}) cm^{-1}. EDS: 0.1:1:0.7 (Rb:Ni:Fe).

Hollow Shell@Shell. $NiCl_2.6H_2O$ (0.40 mmol; 4.0 mM) dissolved in 100 mL of water and an equal volume of an aqueous solution containing $K_3[Cr(CN)_6]$ (0.42 mmol; 4.2 mM) were simultaneously added (8 mL/h using a peristaltic pump) to a 400 mL aqueous solution of the previously synthesized hollow RbCoFe core particles, under vigorous stirring for 18 h. The product was filtered under vacuum using a 0.45 μm filter and washed twice with 500 mL of water. The light purple powder was isolated by centrifugation and air-dried.

$Rb_{0.4}Co_4[Fe(CN)_6]_{2.8}\cdot 7.2H_2O$@$Ni_4[Cr(CN)_6]_{2.7}\cdot 7.8H_2O$ (RbCoFe@NiCr). Light purple powder (97% yield). IR (KBr): 2170 (νCN, Ni^{II}−NC-Cr^{III}) 2157 (νCN, Co^{II}−NC-Fe^{III} HS), 2109 (νCN, Co^{II}−NC-Fe^{III} LS, Co^{II}−NC-Fe^{II}) cm^{-1}. EDS: 0.1:1:0.7:1.2:0.8 (Rb:Co:-Fe:Ni:Cr).

Characterization. Fourier transform infrared spectroscopy (FT-IR) was performed on a Nicolet 6700 Thermo Scientific spectrophotometer taking 32 scans per spectrum between 4000 and 400 cm^{-1} with a precision of 0.482 cm^{-1}. Samples were placed onto the face of a KBr pellet by dispersing 1 mg of powder in methanol or acetone and dropping the dispersion onto the preformed pellet. The spectrum of a pure KBr pellet is taken as a background reference. Transmission electron microscopy (TEM) was performed on a JEOL-2010F high-resolution transmission electron microscope at 200 kV. The TEM samples were prepared by dropping 40 μL of a water or methanol solution (1 mL) containing 2 mg of product, dispersed by sonication, onto the grid (carbon film on a holey carbon support film, 400 mesh, copper from Ted-Pella, Inc.). Energy-dispersive X-ray spectroscopy (EDS) was performed with an Oxford Instruments EDS X-ray Microanalysis System coupled to the high-resolution TEM (HRTEM) microscope. A total of four scans were recorded on different parts of the sample and then averaged to give relative atomic percentages for the metallic elements. Chemical formulas are based on the metal compositions from EDS, adding water as determined by the number of trivalent metal vacancies to ensure charge balance. The particle size distribution is determined from the size measurements of a minimum of 200 particles from multiple regions in one sample. The resulting distributions, with a binning of 1.5 nm for the shell thickness measurements and 3 nm for the particle sizes, are fitted using a log-normal function. Powder X-ray diffraction (PXRD) was performed on a Philips APD 3720 powder diffractometer using a Cu Kα source. Diffractograms were recorded on 25 mg of sample mounted with

dx.doi.org/10.1021/cm302995w | *Chem. Mater.* 2013, 25, 42−47

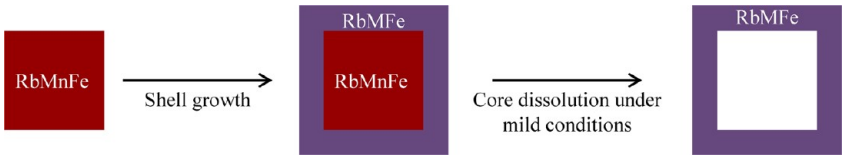

Figure 2. Synthetic strategy consists in preparing core@shell heterostructures with RbMnFe core as a template and RbMFe (M = Co, Ni) as a shell. Dissolution of the template under mild conditions results in the formation of well-preserved hollow shells.

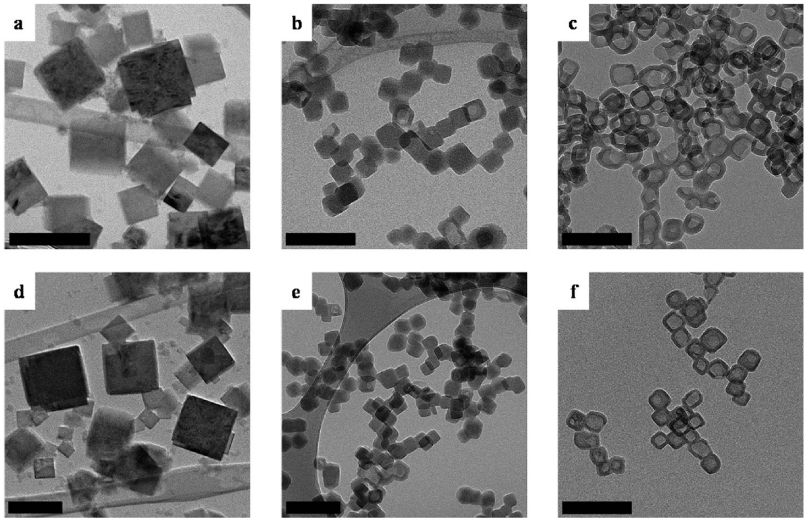

Figure 3. TEM images of RbMnFe cores (a, d) showing polydispersed cubes with a size range of 50 to 300 nm; (b) uniform cubic core@shell particles of RbMnFe@RbCoFe and (e) RbMnFe@RbNiFe; (c) RbCoFe and (f) RbNiFe hollow shells with shape and size preserved upon removal of the template. Shell thickness ranges from 9 to 15 nm. Scale bars for each image are 200 nm.

double-sided tape on a glass slide. Gas sorption measurements were performed on a Micromeritics ASAP 2020 Surface Area Analyzer. RbCoFe (55 mg) was degassed at 95 °C for 20 h and RbNiFe (55 mg) was degassed at 150 °C for 10 h. For each sample, nitrogen sorption measurements were performed at 77 K. Magnetic measurements were performed using a commercial superconducting quantum interference device (SQUID) magnetometer (Quantum Design MPMS-XL7). Powder sample (~1 mg) was immobilized between KBr pellets and mounted in a homemade optic sample rod. The magnetic data were taken after field-cooling in an applied field $\mu_0 H$ = 100 G in warming mode.

RESULTS AND DISCUSSION

Synthesis and Morphology of Hollow RbCoFe and RbNiFe Nanoparticles. Formation of hollow structures via the template method requires differences in physicochemical properties between the shell material or its precursors and the template. Our strategy takes advantage of the increased solubility of RbMnFe PBA compared to other members of the Prussian blue analogue family, known for being quite insoluble. Inspired by the synthesis of PBA core@shell heterostructures previously reported,[29,30] we prepare core@shell particles with the easily dissolved RbMnFe as the core (Figure 2). The RbMnFe cores are synthesized at high concentration of precursors (10−11 mM) in aqueous medium by fast addition of the reagents (2.5 mL/min). These synthetic conditions favor the nucleation process over growth, allowing for the particle size to remain in the nanometric range. The cores are then redispersed in a water/methanol solvent mixture, which limits their dissolution. During the synthesis of the shell, a substoichiometric amount of hexacyanoferrate is added to the divalent metal, inducing an equilibrium shift toward the dissolution of the cores during the synthesis. After the shell growth, the particles are washed in very mild conditions (1 L of water at 45 °C for 45 min) preventing the empty shells from collapsing. An intense yellow color appears in the aqueous wash due to the presence of ferricyanide ions in solution (λ_{max} = 420 nm), confirming the removal and dissolution of the RbMnFe cores.

The morphology and chemical composition of the core, core@shell and hollow shell particles were investigated by TEM (Figure 3) and EDS (Supporting Information). RbMnFe cores are polydispersed cubic particles with sizes ranging from 50 to 300 nm. RbMnFe@RbCoFe and RbMnFe@RbNiFe core@shell particles show a well-defined cubic shape and are nearly uniform in size, 53 ± 12 nm and 52 ± 10 nm, respectively. The chemical assignments and layer segregation within the particles are confirmed by EDS line scans (see Figure S1 in the Supporting Information). The difference in size dispersion compared to the core particles and the presence of hollow structures in the core@shell mixture suggest that partial dissolution of the RbMnFe particles occurs during the shell growth. After the final washing procedure, the hollow morphology of RbCoFe and RbNiFe nanocubes is evident from the sharp difference in contrast between the shell and void space. Moreover, EDS line scans confirm the hollow character of the nanoparticles (see Figure S2 in the Supporting Information). The nanoshells well inherit the narrow size distribution and shape of the core@shell precursors, which supports the retention of the structure upon removal of the template. The thickness of the shells ranges from 9 to 15 nm. In both cases, bulk EDS measurements reveal less than 10% of remaining RbMnFe in the final product.

Powder X-ray diffraction (PXRD) patterns (see the Supporting Information, Figure S3) collected at room temper-

dx.doi.org/10.1021/cm302995w | Chem. Mater. 2013, 25, 42−47

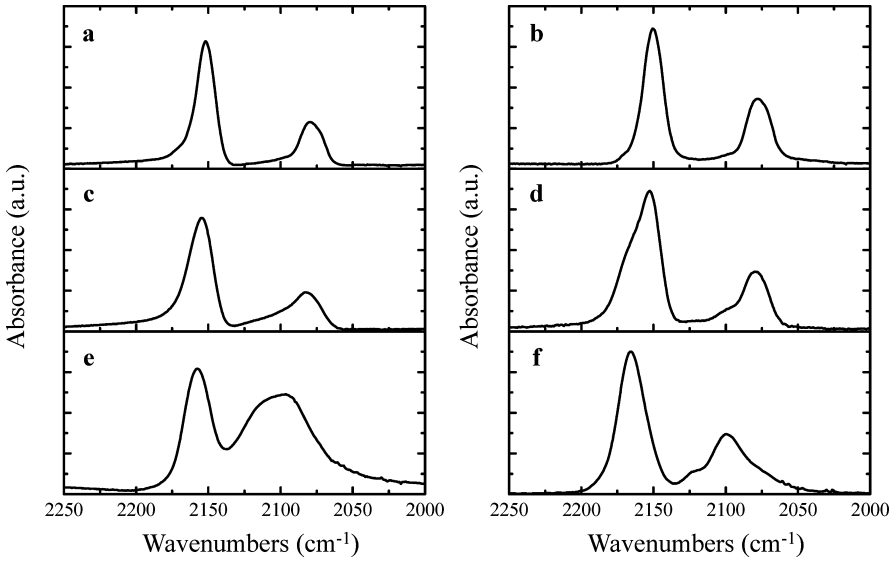

Figure 4. FT-IR spectra for: RbMnFe cores (a, b) exhibiting the two characteristic cyanide stretches from the Mn^{II}–NC–Fe^{III} and Mn^{III}–NC–Fe^{II} sites; RbMnFe@RbCoFe (c) and RbMnFe@RbNiFe (d) core@shells displaying predominant RbMnFe core bands with additional features assigned to the shell material. The difference in intensity between core and shell signals results from a difference in molar extinction coefficients; peaks in spectra of the (e) RbCoFe and (f) RbNiFe hollow shells are characteristic of the pure compounds, supporting the efficient removal of the template.

ature on the RbCoFe and RbNiFe hollow structures can be indexed in the space group $Fm\bar{3}m$ (No. 225) to give lattice constants a = 10.31 Å for RbCoFe and a = 10.17 Å for RbNiFe, consistent with literature precedent.[38,39] Diffraction peak linewidths indicate that the surfactant-free approach to hollow particles yields crystallinity comparable to that seen in bulk preparations.

Analysis of the Templating Process. The RbMnFe sacrificial template plays a dual role in the synthesis. Careful control over the concentration of precursors and the solvent mixture is required to prevent a complete dissolution of the template. However, a change in size and size dispersion occurs from the template as bare particles to the cores embedded in the shells (Figure 3). These observations suggest a dissolution-reprecipitation mechanism of the RbMnFe as the shell grows, which is supported by analyzing mass balance. The yield of hollow nanocubes, calculated from the limiting reagent, $K_3Fe(CN)_6$, is 112% for the RbCoFe hollows and 145% for RbNiFe. These abnormally high values support the partial dissolution, up to 20%, of the RbMnFe template, increasing the concentration of $[Fe(CN)_6]^{3-}$ available in solution for the synthesis of the shell. Although part of the RbMnFe actively contributes to the shell growth, the remaining template cores can be dissolved by a gentle wash to obtain the hollow structures.

Following each synthetic step by FT-IR gives insight into the evolution of the chemical makeup during subsequent steps in the synthesis. The FT-IR spectra, shown in the cyanide stretching region for the RbMnFe cores (Figure 4), display two bands at 2151 and 2080 cm^{-1} characteristic of, respectively, both Mn^{II}–NC–Fe^{III} and Mn^{III}–NC–Fe^{II} sites in the network.[35] After the shell synthesis, the RbMnFe peaks remain predominant in the FT-IR spectra for the core@shell samples because of differences in the molar extinction coefficients. However, additional features appear confirming the presence of a new material. The broad and asymmetric signal at 2152 cm^{-1} arises from two overlapping bands corresponding to the Mn^{II}–NC–Fe^{III} stretching of the core and Co^{II}–NC–Fe^{III} or Ni^{II}–NC–Fe^{III} forms in the shell compounds. Moreover, in both cases, a shoulder emerges on the high energy side of the core band at 2080 cm^{-1}, which can be assigned to characteristic cyanide stretches in the shell material: at 2109 cm^{-1} for RbCoFe and at 2099 cm^{-1} for RbNiFe. Strikingly, the FT-IR spectra of the hollow structures are characteristic of the pure shell materials, supporting the nearly complete dissolution of the RbMnFe template. For the RbCoFe nanoshells, the FT-IR spectrum exhibits a peak at 2159 cm^{-1} and a broad asymmetric signal defining peaks at 2109 cm^{-1}, corresponding to Co^{II}–NC–Fe^{III}, and at 2095 cm^{-1}, characteristic of the Co^{II}–NC–Fe^{II} reduced form of the compound.[36] The FT-IR spectrum of the RbNiFe hollow shells displays peaks at 2165 and 2124 cm^{-1}, attributed to the bridging and terminal cyanides of Ni^{II}–NC–Fe^{III}, as well as a band at 2099 cm^{-1} characteristic of the Ni^{II}–NC–Fe^{II} reduced phase.[37]

Properties of the Hollow Particles. *Porosity.* The pore sizes and surface areas of the hollow particles were analyzed via nitrogen gas sorption studies (see the Supporting Information, Figure S4). The N_2 adsorption–desorption isotherms measured at 77 K clearly show pseudo type IV behavior, indicating the organization of hierarchical pores as expected for the PBA hollow shells. The steep uptake followed by a plateau before P/P_0 = 0.1 is related to the pore filling of the micropores within the PBA framework, while the observed hysteresis in the pressure range of P/P_0 = 0.5–1 is indicative of mesopores resulting from the hollow morphology. By applying the Brunauer–Emmett–Teller (BET) model, the specific surface area is calculated to be 694 m^2/g for RbCoFe and 786 m^2/g for RbNiFe, both of which are consistent with previously reported values for PBAs with a similar M/M′ metal ratio.[40,41] Literature precedents indicate a value of 277 m^2/g for hollow CoFe synthesized by controlled chemical etching.[34] The higher value observed for the RbCoFe hollows described here suggests improved crystallinity of the shells using this surfactant-free approach. Micropore size distribution analysis based upon a Density Functional Theory (DFT) model reveals that the pores of RbCoFe and RbNiFe are predominantly distributed around

dx.doi.org/10.1021/cm302995w | *Chem. Mater.* 2013, 25, 42–47

8.5 Å, which is in good agreement with expected cyanometallate vacancies in the PBA lattice. Barrett–Joyner–Halenda (BJH) mesopore distribution analysis indicates a maximum around 38 Å for both compounds and the mesopores presumably originate from the defects in the crystalline shell. The well-defined pores and high surface areas suggest that the integrity of the PBA structure remains intact upon dehydration.

Surface Reactivity. The synthetic strategy has the major advantage of being surfactant-free. As a result, the reactivity of the PBA surface, with its terminal cyanides and acidic sites, is preserved. To illustrate the reactivity of the shell, hollow shell@shell heterostructures were prepared. RbCoFe hollow shells were used as precursors for the growth of a NiCr PBA layer. TEM images (Figure 5) show well-defined cubic hollow

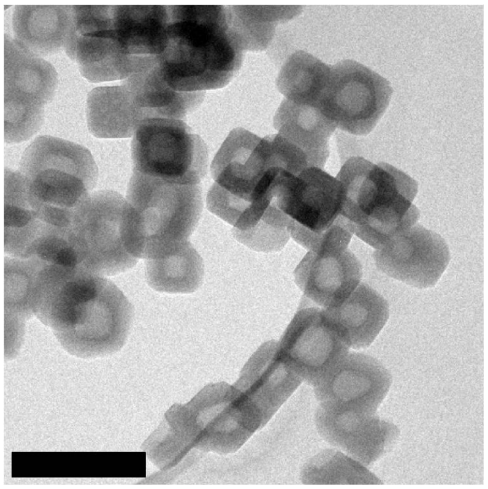

Figure 5. TEM image of hollow nanocubes with a shell thickness of 23 ± 6 nm. Although the shell thickens from the pure hollow shell to the heterostructure, the void size remains constant, suggesting the NiCr deposits on the surface of the RbCoFe hollow precursor. The scale bar is 200 nm.

particles with a shell thickness of 23 ± 6 nm compared to 11 ± 4 nm for the starting hollow RbCoFe particles. The chemical assignments and layer segregation within the particles are confirmed by EDS line scans (see Figure S5 in the Supporting Information). Whereas the shell significantly thickens from the pure RbCoFe hollow precursor to the RbCoFe@NiCr heterostructure, the void size remains constant, which indicates a growth from the outer surface of the nanocubes. Moreover, the Ni/Co atomic ratio obtained by bulk EDS correlates with the layer thickness ratio as expected in the absence of side nucleation. Hence, these observations suggest the NiCr deposits on the surface of the hollow precursors without side nucleation. Whereas the FT-IR spectrum of the hollow shells is characteristic of pure RbCoFe, the cyanide stretch region of the hollow shell@shells shows an additional signal at 2170 cm^{-1} attributed to Ni^{II}–NC–Cr^{III} (Figure 6).

Further evidence of the presence of two segregated layers as opposed to a mixed material can be found in the magnetic behavior of the hollow shell@shell. The field-cooled magnetization vs temperature plot (Figure 7) exhibits two ordering temperatures, T_c = 20 K and T_c = 75 K, assigned, respectively, to the ferrimagnetic ordering in RbCoFe and ferromagnetic ordering of NiCr.[42,43] These two distinct ordering temperatures are indicative of two noninteracting materials, confirming the growth of the NiCr layer on top of the RbCoFe shell with little

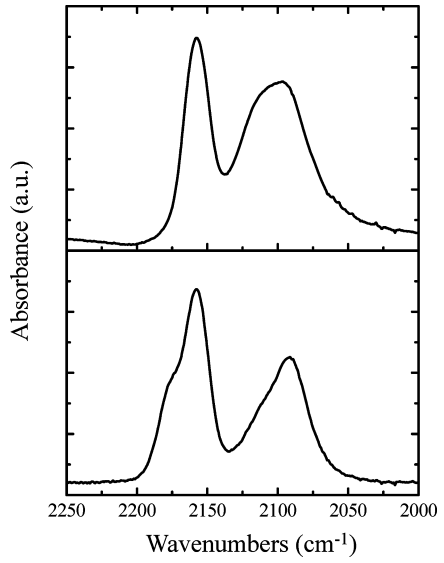

Figure 6. FT-IR spectra for RbCoFe hollow shells (top) and RbCoFe@NiCr hollow heterostructures (bottom), with additional band at 2170 cm^{-1} assigned to the Ni^{II}–NC–Cr^{III} sites.

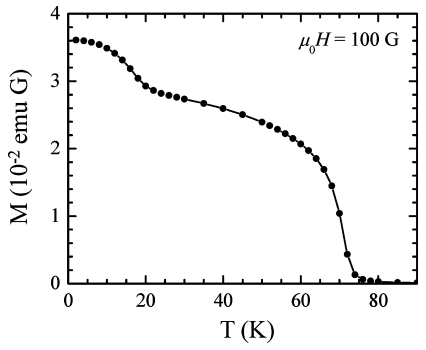

Figure 7. Magnetization vs temperature plot in an applied magnetic field $\mu_0 H$ = 100 G exhibits two distinct ordering temperatures characteristic of the RbCoFe (T_c = 20 K) and NiCr (T_c = 75 K) shells, which confirms the segregation of layers within the nanoparticles.

mixing of ions from the two components. The ability to grow a second layer of a different PBA on the hollow nanocubes proves their reactivity toward further chemical modification. Although the hollow shell@shell particles were irradiated in a manner that generates photoinduced magnetism in core@shell samples,[30] these experiments showed no evidence of photo-induced effects for the hollow heterostructures. The chemical formula of the RbCoFe shells indicates a high number of cyanometallate vacancies in the structure that hinders the bistabily required to observe the photoinduced magnetization.[36,38]

■ CONCLUSION

RbCoFe and RbNiFe PBA hollow nanocubes were successfully prepared via a facile surfactant-free route using RbMnFe as a removable template. The hollow structured nanoparticles are crystalline and nearly uniform in size. With their high surface area and the presence of well-defined micro- and mesopores in the shell enclosing the larger cavity, these materials provide illustrative examples of multilevel pore systems. Furthermore, the preparation of self-stabilized colloidal suspensions allows for the design of exotic coordination polymer heterostructures.

dx.doi.org/10.1021/cm302995w | *Chem. Mater.* 2013, 25, 42–47

Such a hierarchical porous architecture added to a reactive and magnetic shell is promising for applications in adsorptive/magnetic separation. The loading of such magnetic porous nanoparticles with functional molecules would be of great interest for targeted drug delivery or selective catalysis.

■ ASSOCIATED CONTENT

Supporting Information

(1) EDS line scans on RbMnFe@RbCoFe and RbMnFe@RbNiFe core@shell particles; (2) EDS line scans on RbCoFe hollow shells; (3) PXRD patterns for RbCoFe and RbNiFe hollow shells; (4) nitrogen sorption analysis with pore size distribution in RbCoFe and RbNiFe hollow nanocubes determined by DFT and BJH models; (5) EDS line scans on a RbCoFe@RbNiCr shell@shell particle. This material is available free of charge via the Internet at http://pubs.acs.org/.

■ AUTHOR INFORMATION

Corresponding Author

*E-mail: talham@chem.ufl.edu.

Notes

The authors declare no competing financial interest.

■ ACKNOWLEDGMENTS

This work was supported by the National Science Foundation through grants DMR-1005581 (D.R.T.) and DMR-1202033 (M.W.M.). The authors thank the University of Florida Major Analytical Instrument Center for access to TEM imaging and EDS analysis.

■ REFERENCES

(1) Davis, M. E. *Nature* **2002**, *417*, 813−821.
(2) Bradshaw, D.; Claridge, J. B.; Cussen, E. J.; Prior, T. J.; Rosseinsky, M. J. *Acc. Chem. Res.* **2005**, *38*, 273−282.
(3) Zhao, Y.; Jiang, L. *Adv. Mater.* **2009**, *21*, 3621−3638.
(4) Lopez-Orozco, S.; Inayat, A.; Schwab, A.; Selvam, T.; Schwieger, W. *Adv. Mater.* **2011**, *23*, 2602−2615.
(5) Lou, X. W.; Archer, L. A.; Yang, Z. *Adv. Mater.* **2008**, *20*, 3987−4019.
(6) Ameloot, R.; Vermoortele, F.; Vanhove, W.; Roeffaers, M. B. J.; Sels, B. F.; De, V. D. E. *Nat. Chem.* **2011**, *3*, 382−387.
(7) Ding, S.; Chen, J. S.; Qi, G.; Duan, X.; Wang, Z.; Giannelis, E. P.; Archer, L. A.; Lou, X. W. *J. Am. Chem. Soc.* **2011**, *133*, 21−23.
(8) Wang, Z.; Luan, D.; Boey, F. Y. C.; Lou, X. W. D. *J. Am. Chem. Soc.* **2011**, *133*, 4738−4741.
(9) Zhu, Y.; Shi, J.; Shen, W.; Dong, X.; Feng, J.; Ruan, M.; Li, Y. *Angew. Chem., Int. Ed.* **2005**, *44*, 5083−5087.
(10) Caruso, F.; Caruso, R. A.; Moehwald, H. *Science* **1998**, *282*, 1111−1114.
(11) Kim, S.-W.; Kim, M.; Lee, W. Y.; Hyeon, T. *J. Am. Chem. Soc.* **2002**, *124*, 7642−7643.
(12) Sun, Y.; Xia, Y. *Science* **2002**, *298*, 2176−2179.
(13) Yin, Y.; Rioux, R. M.; Erdonmez, C. K.; Hughes, S.; Somorjai, G. A.; Alivisatos, A. P. *Science* **2004**, *304*, 711−714.
(14) Zoldesi, C. I.; Imhof, A. *Adv. Mater.* **2005**, *17*, 924−928.
(15) Peng, Q.; Dong, Y.; Li, Y. *Angew. Chem., Int. Ed.* **2003**, *42*, 3027−3030.
(16) Lee, H. J.; Cho, W.; Oh, M. *Chem. Commun.* **2012**, *48*, 221−223.
(17) Liang, G.; Xu, J.; Wang, X. *J. Am. Chem. Soc.* **2009**, *131*, 5378−5379.
(18) Huo, J.; Wang, L.; Irran, E.; Yu, H.; Gao, J.; Fan, D.; Li, B.; Wang, J.; Ding, W.; Amin, A. M.; Li, C.; Ma, L. *Angew. Chem., Int. Ed.* **2010**, *49*, 9237−9241.
(19) Roy, X.; Hui, J. K. H.; Rabnawaz, M.; Liu, G.; MacLachlan, M. J. *J. Am. Chem. Soc.* **2011**, *133*, 8420−8423.
(20) Chae, H. K.; Siberio-Perez, D. Y.; Kim, J.; Go, Y. B.; Eddaoudi, M.; Matzger, A. J.; O'Keeffe, M.; Yaghi, O. M. *Nature* **2004**, *427*, 523−527.
(21) Furukawa, H.; Ko, N.; Go, Y. B.; Aratani, N.; Choi, S. B.; Choi, E.; Yazaydin, A. O.; Snurr, R. Q.; O'Keeffe, M.; Kim, J.; Yaghi, O. M. *Science* **2010**, *329*, 424−428.
(22) Betard, A.; Fischer, R. A. *Chem. Rev.* **2012**, *112*, 1055−1083.
(23) Kreno, L. E.; Leong, K.; Farha, O. K.; Allendorf, M.; Van, D. R. P.; Hupp, J. T. *Chem. Rev.* **2012**, *112*, 1105−1125.
(24) Verdaguer, M..; Girolami, G. S. *Magnetic Prussian Blue Analogs in Magnetism: Molecules to Materials V*; Miller, J. S., Dorillon, M., *Eds.*; Wiley-VCH: New York, 2005.
(25) Ludi, A.; Güdel, H. U. *Struct. Bonding (Berlin)* **1973**, *14*, 1−21.
(26) Vaucher, S.; Fielden, J.; Li, M.; Dujardin, E.; Mann, S. *Nano Lett.* **2002**, *2*, 225−229.
(27) Yamada, M.; Sato, T.; Miyake, M.; Y., K. *J. Colloid Interface Sci.* **2007**, *315*, 369−375.
(28) Brinzei, D.; Catala, L.; Louvain, N.; Rogez, G.; Stephan, O.; Gloter, A.; Mallah, T. *J. Mater. Chem.* **2006**, *16*, 2593−2599.
(29) Catala, L.; Brinzei, D.; Prado, Y.; Gloter, A.; Stephan, O.; Rogez, G.; Mallah, T. *Angew. Chem., Int. Ed.* **2009**, *48*, 183−187.
(30) Dumont, M. F.; Knowles, E. S.; Guiet, A.; Pajerowski, D. M.; Gomez, A.; Kycia, S. W.; Meisel, M. W.; Talham, D. R. *Inorg. Chem.* **2011**, *50*, 4295−4300.
(31) Prado, Y.; Dia, N.; Lisnard, L.; Rogez, G.; Brisset, F.; Catala, L.; Mallah, T. *Chem. Commun.* **2012**, *48*, 11455−11457.
(32) McHale, R.; Ghasdian, N.; Liu, Y.; Ward, M. B.; Hondow, N. S.; Wang, H.; Miao, Y.; Brydson, R.; Wang, X. *Chem. Commun.* **2010**, *46*, 4574−4576.
(33) Hu, M.; Furukawa, S.; Ohtani, R.; Sukegawa, H.; Nemoto, Y.; Reboul, J.; Kitagawa, S.; Yamauchi, Y. *Angew. Chem., Int. Ed.* **2012**, *51*, 984−988.
(34) Hu, M.; Torad, N. L.; Yamauchi, Y. *Eur. J. Inorg. Chem.* **2012**, 4795−4799.
(35) Ohkoshi, S.; Matsuda, T.; Tokoro, H.; Hashimoto, K. *Chem. Mater.* **2005**, *17*, 81−84.
(36) Bleuzen, A.; Lomenech, C.; Escax, V.; Villain, F.; Varret, F.; Cartier, d. M. C.; Verdaguer, M. *J. Am. Chem. Soc.* **2000**, *122*, 6648−6652.
(37) Sato, O. *J. Solid State Electrochem.* **2007**, *11*, 773−779.
(38) Shimamoto, N.; Ohkoshi, S.; Sato, O.; Hashimoto, K. *Inorg. Chem.* **2002**, *41*, 678−684.
(39) Choudhury, S.; Bagkar, N.; Dey, G. K.; Subramanian, H.; Yakhmi, J. V. *Langmuir* **2002**, *18*, 7409−7414.
(40) Kaye, S. S.; Long, J. R. *J. Am. Chem. Soc.* **2005**, *127*, 6506−6507.
(41) Karadas, F.; El-Faki, H.; Deniz, E.; Yavuz, C. T.; Aparicio, S.; Atilhan, M. *Microporous Mesoporous Mater.* **2012**, *162*, 91−97.
(42) Sato, O.; Iyoda, T.; Fujishima, A.; Hashimoto, K. *Science* **1996**, *272*, 704−5.
(43) Gadet, V.; Mallah, T.; Castro, I.; Verdaguer, M.; Veillet, P. *J. Am. Chem. Soc.* **1992**, *114*, 9213−14.